Int J Adv Manuf Technol (2014) 71:753–773
DOI 10.1007/s00170-013-5518-4

ORIGINAL ARTICLE

Global sensitivity analysis and multi-objective optimisation of loading path in tube hydroforming process based on metamodelling techniques

Anis Ben Abdessalem · Abdelkhalak El-Hami

Received: 19 July 2013 / Accepted: 19 November 2013 / Published online: 11 December 2013

Abstract Tube hydroforming process is widely used in various industrial applications which consists of combining internal pressure and axial displacement to manufacture tubular parts. Inappropriate choice as small changes in such variables may affect the process stability and, in some cases, lead to failure. Consequently, loading path should be optimised to better control the process and to guarantee hydroformed parts with desired specifications. However, optimisation procedure requires several evaluations of the real models which induces a huge computational time. To cope with this limitation, we propose to compare two metamodelling techniques to solve the problem efficiently: the response surface method and the least squares support vector regression. To enhance the metamodels precision, optimal latin hypercube design is used to generate sampled points. It is obtained through iterative optimisation procedure based on a modified version of the simulated annealing algorithm by minimising simultaneously two optimality criterions. Then, multi-objective optimisation problem is formulated to search for the Pareto optimal solutions. Fuzzy classification is then applied to rank the non-dominated solutions which helps designers in the decision-making phase. Before optimising the process, a global sensitivity analysis is carried out using the variance-based method by coupling metamodels and Monte Carlo simulations in order to identify the relative importance of the design variables in terms of internal pressure and axial displacement on the variance of the responses of interest defined to control the process.

Keywords Tube hydroforming process · Loading path · Metamodelling · Global sensitivity analysis · Monte Carlo simulations · Multi-objective optimisation · Pareto front

1 Introduction

Hydroforming (HF) processes have been extensively used to manufacture a variety of components in the automotive industry [1–3] and is of increasing interest to other industries as well. They represent an excellent way of manufacturing simple and complex parts with a high level of repeatability, lower tooling cost and higher dimensional accuracy. Generally, HF processes can be divided into two broad categories: tube hydroforming (THF) process and sheet hydroforming process, each characterised primarily by the specific applied loads and involved tools. In the present research, we focus only on THF process where the tube is simultaneously subjected to a uniformly distributed internal pressure and axial displacement. A successful hydroforming operation requires precise selection of loading path which depends essentially on material properties, geometric characteristics and frictional conditions. Selecting an appropriate loading path without any a priori knowledge about the problem is a very hard task for engineers. So either we need some kind of trial-and-error adjustment or we adopt some finite element (FE) simulations based on reliable FE model coupled with iterative optimisation method. The latter appears more appropriate

A. Ben Abdessalem (✉)
Université de Bordeaux, I2M, UMR CNRS 5295, 351 Cours de la Libération, 33405 Talence Cedex, France
e-mail: anis.ben-abdessalem@u-bordeaux1.fr

A. El-Hami
INSA de Rouen, LOFIMS, B.P. 8, Avenue de l'Université, 76801 St Etienne du Rouvray, France

since the former is very costly mostly for complex components. Additionally, the use of this approach has been widely adopted in the literature and its robustness has been demonstrated through several studies. In the following, we will present the recent interesting methods applied for optimising THF process for various components with different geometry.

During the last decade, several papers have been published with the aim to optimise loading path in THF process. The most proposed strategies are based on the finite element analysis (FEA) coupled with an optimisation procedure. They differ mainly in the optimisation algorithm chosen (meta-heuristic algorithms, gradient-based algorithms, hybrid optimisation methods, etc.) and the selected failure criterions used to control the process. Ray and Mac Donald [4] proposed to optimise loading path for THF process using a fuzzy load control algorithm and FEA. The proposed algorithm is used in conjunction with LS-DYNA FE code for simulation of the forming process. An et al. [5] used a multi-objective optimisation algorithm combined with the Taguchi statistical method and FEA to determine optimal loading path for a simple THF process. Ingarao et al. [6] proposed a multi-objective approach to design a complex Y-shaped tube hydroforming. These authors investigated the calibration of internal pressure and counter punch action to achieve three different quality objectives: minimisation of thinning, reduction of underfilling and accuracy of the final fillet radius at the bulge zone corner. Lin and Kwan [7] applied abductive network and finite element method (FEM) to manufacture an acceptable product of which wall thickness and the protrusion height fulfil the industrial demand on the T-shape THF process. Mirzaali et al. [8] used the simulated annealing algorithm as meta-heuristic method to optimise loading path in THF process. Xu et al. [9] investigated the effects of the loading path on the hydroformability of trapezoid-sectional parts. Through numerical simulations, the effects of die angles and friction coefficients on the hydroforming process and the final parts are explored. Zadeh and Mashhadi [10] investigated the formability of unequal T-joints by FE simulations and experiments. These authors showed that there is a good agreement between FEM and experimental results. Alaswad et al. [11] used the response surface (RS) models to investigate the effects of geometrical factors on branch height and thickness reduction in T-shape bi-layered THF process. Abedrabbo et al. [12] proposed an optimisation method linked with the FEM to optimise internal hydraulic pressure and end feed rate, while satisfying the failure limits defined by the forming limit diagram (FLD). Di Lorenzo et al. [13] proposed a gradient-based decomposition approach which consists in reducing the required numerical simulations about 50 % to optimise internal pressure and counter punch action in Y-shaped THF operation. The basic idea is focused on the possibility to decompose the design variables space in subdomains which simplify significantly the problem.

The aforementioned strategies have been successfully applied for optimising THF process; however, optimisation of such process which have to consider various objective functions and constraints, requires often large computational time, even when using reduced FE model. Implicit functions have to be evaluated for many times to explore the search space. To cope with this problem, metamodels which consist in finding a functionals relations between the responses of interest and selected process parameters to be optimised are widely adopted to solve numerous metal forming processes [14–20] and in particular THF process [21–23]. The use of the metamodels is particularly important when the optimisation procedure requires several evaluations of the objective functions and constraints via FE simulations which induce excessive computational time. This alternative allows to reduce considerably the time consumption and provides an optimal solution with reasonable cost. However, it is important to mention that a careful attention should be paid to this stage since the robustness and the reliability of the optimal solution is directly dependent on the ability of the selected metamodels to better approximate the real function. Sophisticated metamodels are often required mainly when the problem presents several sources of nonlinearities as the THF process. In this work, we propose to investigate the capability of the traditional response surface method (RSM) and the least squares support vector regression (LSSVR). The LSSVR has been recently introduced into various disciplines and it is proving to be a very promising general regression technique. Several studies [24–26] have successfully applied the LSSVR for function approximation in different areas for nonlinear problems. For enhancing the metamodels capability, both metamodelling techniques are coupled with optimal latin hypercube design (LHD) obtained with consideration of two optimality criterions: minimising the correlation between design variables vectors and maximising the minimum distances between variables in the design space. Then, the problem is solved with a modified version of the simulated annealing (SA) algorithm. This strategy allows an optimal distribution of the sampled points in the design space and consequently to improve the performance of the metamodels for reliable prediction.

It should be noted that for all the optimisation strategies discussed previously, it might be hard to discuss about which one is superior because in different metal forming processes or even in a same process with different variables, these methods will perform variously. Consequently, the problem formulation is always a difficult task mainly when several desired specifications should be satisfied. In THF process, it is always desirable to simultaneously optimise several opposing design objectives. For this reason, multi-objective optimisation formulation appears more adequate to formulate the problem under consideration. Before dealing with optimisation, a global sensitivity analysis (GSA) is performed based on the generated metamodels and Monte Carlo simulations (MCS) by assuming random the design variables. GSA allows to identify the most important variables which have the highest contribution to the variance of the specified output defined to control the process. In addition, GSA investigates the interaction effects between the design variables involved in the THF process.

The organisation of the paper is as follows. In Section 2, we introduce the basic concepts of the RSM and the LSSVR metamodelling techniques, then their prediction capability is investigated and compared through nonlinear test function. In Section 3, we introduce the numerical example proposed to optimise the THF process as the main objective functions defined to control the process. Global sensitivity analysis using the variance-based method is detailed and discussed in Section 4. In Section 5, multi-objective optimisation problem is formulated and the obtained results are analysed and discussed. In the final section, some concluding remarks are drawn and future research directions are proposed.

2 Metamodelling techniques and design of experiment

2.1 Response surface methodology

The RS model can be stated as follows in its general form:

$$z = \tilde{z} + e = \sum_{i=1}^{L} \beta_i \psi_i(\mathbf{x}) + e, \tag{1}$$

where z denotes the true response, $\tilde{z}$ is the RS model, e is the approximation error, $\mathbf{x}$ is a vector of design variables and β_i $(i = 1, \ldots, L)$ is the ith unknown coefficients corresponding to the ith basis function $\psi_i(\mathbf{x})$.

The choice of the basis function depends directly on the nature and the complexity of the problem to be solved. The quadratic polynomial RS model given by Eq. (2) and used in the present work was commonly adopted in solving various metal forming processes as mentioned previously.

$$\tilde{z} = \beta_0 + \sum_{i=1}^{m} \beta_i \mathcal{X}_i + \sum_{i=1}^{m} \beta_i {\mathcal{X}_i}^2 + \sum_{i=1}^{m-1} \sum_{j=i+1}^{m} \beta_{ij} \mathcal{X}_i \mathcal{X}_j \tag{2}$$

where the unknown parameters $\boldsymbol{\beta} = [(\beta_0, \beta_1, \ldots, \beta_L)]^{\mathrm{T}}$ can be determined by means of the least squares method (The symbol "T" denotes the transpose operation) and m is the total number of the design variables involved in the model.

At the ith design points $\mathbf{x}_i$, the error between the actual and the predicted values is expressed as:

$$e_i = z^{(i)} - \tilde{z}^{(i)} = z^{(i)} - \sum_{j=1}^{L} \beta_j \psi_j(\mathbf{x}_i). \tag{3}$$

The objective is to minimise the total squared error between the actual and the predicted values which is called the least squares regression, let define $\mathcal{Q}(\boldsymbol{\beta})$ as:

$$\mathcal{Q}(\boldsymbol{\beta}) = \sum_{i=1}^{n_\mathrm{d}} e_i^2 = \sum_{i=1}^{n_\mathrm{d}} \left[z^{(i)} - \sum_{j=1}^{L} \beta_j \psi_j(\mathbf{x}_i) \right]^2 \tag{4}$$

where n_d is the number of the design points used to identify the coefficients model.

Equation (4) can be transformed in matrix notation as follows:

$$\mathcal{Q}(\boldsymbol{\beta}) = (z - \boldsymbol{\psi}\boldsymbol{\beta})^{\mathrm{T}}(z - \boldsymbol{\psi}\boldsymbol{\beta}) \tag{5}$$

Then, the error is minimised by setting to zero the derivatives $\frac{\partial \mathcal{Q}(\boldsymbol{\beta})}{\partial \boldsymbol{\beta}}$, the following expression can be derived:

$$\boldsymbol{\beta} = [\boldsymbol{\psi}^{\mathrm{T}}\boldsymbol{\psi}]^{-1}\boldsymbol{\psi}^{\mathrm{T}} z = \boldsymbol{\psi}^{*} z \tag{6}$$

where $\boldsymbol{\psi}^{*}$ is the so called pseudo-inverse matrix of $\boldsymbol{\psi}$ and the fitted values can be computed as:

$$\hat{\boldsymbol{z}} = \boldsymbol{\psi}\boldsymbol{\beta} \tag{7}$$

2.2 Basic concept of the LSSVR

The LSSVR is a modified version of the support vector regression (SVR) [27] used to approximate an unknown function using the set of n_u samples $\{(\boldsymbol{\mathcal{X}}_k, \mathrm{y}_k), k = 1, \ldots, n_u\}$. The regression function can be formulated as follows:

$$f(\boldsymbol{\mathcal{X}}) = \boldsymbol{\omega}^{\mathrm{T}}\varphi(\boldsymbol{\mathcal{X}}) + b, \tag{8}$$

where $\varphi(\cdot)$ denotes the feature of the inputs, and $\boldsymbol{\omega}$ and b indicate the coefficients. The LSSVR introduces a least squares version of the SVR by formulating the regression problem as:

$$\begin{aligned} &\underset{\boldsymbol{\omega},b,\boldsymbol{e}}{\text{Minimise}} \quad \mathcal{J}(\boldsymbol{\omega}, \boldsymbol{e}) = \frac{1}{2}\boldsymbol{\omega}^{\mathrm{T}}\boldsymbol{\omega} + \frac{C}{2}\sum_{k=1}^{n_u} e_k^2 \\ &\text{subject to}: \ \mathcal{X}_k = \boldsymbol{\omega}^{\mathrm{T}}\varphi(\boldsymbol{\mathcal{X}}_k) + b + e_k, \quad k = 1, 2, \ldots, n_u \end{aligned} \tag{9}$$

where $C \geq 0$ denotes the regularization parameter and e_k represents the error. The primal problem is difficult to solve as $\boldsymbol{\omega}$ is high dimensional. Therefore, let us proceed by constructing the Lagrangian and derive the dual problem as follows:

$$\mathcal{L}(\boldsymbol{\omega}, b, \boldsymbol{e}; a) = \mathcal{J}(\boldsymbol{\omega}, \boldsymbol{e}) - C \sum_{k=1}^{n_u} a_l \left[\boldsymbol{\omega}^{\mathrm{T}} \varphi(\mathcal{X}_k) + b + e_k - \mathrm{y}_k\right] \quad (10)$$

Conditions for optimality can be obtained by calculating the partial derivatives with respect to all components of ($\boldsymbol{\omega}$, b, e, a) and setting them to zero as follows:

$$\begin{cases} \dfrac{\partial \mathcal{L}}{\partial \boldsymbol{\omega}} = 0 \Rightarrow \boldsymbol{\omega} = \displaystyle\sum_{k=1}^{n_u} a_k \varphi(\boldsymbol{\mathcal{X}}_k) \\ \dfrac{\partial \mathcal{L}}{\partial b} = 0 \Rightarrow \displaystyle\sum_{k=1}^{n_u} a_k = 0 \\ \dfrac{\partial \mathcal{L}}{\partial e_k} = 0 \Rightarrow a_k = C e_k, \quad k = 1, \ldots, n_u \\ \dfrac{\partial \mathcal{L}}{\partial a_k} = 0 \Rightarrow \mathrm{y}_k = \boldsymbol{\omega}^{\mathrm{T}} \varphi(\boldsymbol{\mathcal{X}}_k) + b + e_k, \quad k = 1, \ldots, n_u \end{cases} \quad (11)$$

After elimination of $\boldsymbol{\omega}$ and e, the solution is obtained as:

$$\begin{bmatrix} 0 & \mathbf{1}^{\mathrm{T}} \\ \mathbf{1} & \Gamma + \frac{1}{C} I \end{bmatrix} \begin{bmatrix} b \\ a \end{bmatrix} = \begin{bmatrix} 0 \\ \mathbf{y} \end{bmatrix} \quad (12)$$

where $\mathbf{y}_k = [\mathrm{y}_1, \ldots, \mathrm{y}_{n_u}]^{\mathrm{T}}$, $\mathbf{1} = [1, \ldots, 1]^{\mathrm{T}}$, $\boldsymbol{a} = [a_1, \ldots, a_{n_u}]^{\mathrm{T}}$, and I is an identity matrix. The kernel trick is applied here as follows:

$$\Omega_{kl} = \varphi(\boldsymbol{\mathcal{X}}_k)^{\mathrm{T}} \varphi(\boldsymbol{\mathcal{X}}_l) = \boldsymbol{\kappa}(\boldsymbol{\mathcal{X}}_k, \boldsymbol{\mathcal{X}}_l) \ \text{ for } \ k, l = 1, 2, \ldots, n_u \quad (13)$$

where $\boldsymbol{\kappa}$ $(\boldsymbol{\mathcal{X}}_k, \boldsymbol{\mathcal{X}}_l)$ is the kernel function.

In this paper, two types of kernel functions, namely the polynomial function (PL) and the radial basis function (RBF) were employed to investigate their prediction capability. The analytical expressions of the PL and the RBF kernel functions are given by Eqs. (14) and (15), respectively:

$$\boldsymbol{\kappa}(\boldsymbol{\mathcal{X}}_k, \boldsymbol{\mathcal{X}}_l) = \left(\boldsymbol{\mathcal{X}}_k{}^{\mathrm{T}} \boldsymbol{\mathcal{X}}_{l+t^d}\right) \quad (14)$$

$$\boldsymbol{\kappa}(\boldsymbol{\mathcal{X}}_k, \boldsymbol{\mathcal{X}}_l) = \exp\left(\frac{-\|\boldsymbol{\mathcal{X}}_k - \boldsymbol{\mathcal{X}}_l\|^2}{\sigma^2}\right) \quad (15)$$

We can get a and b from Eq. (12), therefore, the result of the LSSVR model is:

$$f(\boldsymbol{\mathcal{X}}) = \sum_{k=1}^{n_u} a_k \boldsymbol{\kappa}(\boldsymbol{\mathcal{X}}, \boldsymbol{\mathcal{X}}_k) + b \quad (16)$$

It is important to mention that the performance of the LSSVR relies significantly on the appropriate choice of the kernel functions parameters. In this work, simplex algorithm has been used to fine-tuning the parameters for both kernel functions.

2.3 Optimal latin hypercube design

The choice of the design of experiment (DOE) plays a key role in the accuracy and robustness of the approximation models. There are many different experimental design methods available such as full factorial, latin hypercube, central composite, and so on. Among the mentioned ones, the LHD has excellent performance of capturing the higher order of nonlinearity. However, a random LHD can be quite structured in which the generated points in the design space may be highly correlated or may not have good space-filling properties. To cope with these limitations, two optimality criterions are combined for searching the optimal one in which the metamodels will be estimated. There are different strategies proposed in the literature for finding a good LHD, the most popular ones consist in minimising the pairwise correlations and maximising the inter-site distances. In this work, we propose to combine the previous criterions in one objective to find the optimal LHD.

Let us denote by $\mathcal{D}(n_v, \zeta)$ the initial random LHD with n_v realisations and ζ factors. The first optimality criterion which measures the correlation between all factors is defined as follows:

$$\rho^2 = \frac{\displaystyle\sum_{i=2}^{\zeta} \sum_{j=1}^{i-1} \rho_{ij}^2}{\zeta(\zeta - 1)2^{-1}} \quad (17)$$

where ρ_{ij} is the linear correlation between columns i and j, notice that $\rho^2 \in [0,1]$.

The second criterion is expressed by means of the distances $d(\mathrm{x}_i, \mathrm{x}_j)$ in the design space between any two points denoted by x_i and x_j. It is used to achieve better space-filling property, it consists in maximising the minimum inter-site distance as follows:

$$\underset{1 \le i, j \le n_v, i \ne j}{\text{maximin}} \qquad d(\mathrm{x}_i, \mathrm{x}_j) \quad (18)$$

where $d(\mathrm{x}_i, \mathrm{x}_j)$ is the distance between two sample points x_i and x_j evaluated as follows:

$$d(\mathrm{x}_i, \mathrm{x}_j) = d_{ij} = \left[\sum_{\zeta=1}^{n_v} \mid x_{i\zeta} - x_{j\zeta} \mid^2\right]^{1/2} \tag{19}$$

In our contribution, the formulation of maximin distance proposed by Morris and Mitchell [28] is adopted for searching the optimal LHD. This criterion is based on the inter-points distances evaluated by means of Eq. (19). For a given design, let us define a distance list $d = (d_1, d_2, \ldots, d_\ell)$ in which the elements are the distinct values of inter-points distances, ranked in ascending order. Let J_i be the number of pairs in the design that have distance d_i. Then a design $\mathcal{D}_i$ is called a maximin design if it sequentially maximises d_i's and minimises J_i's in the following order: $(d_1, J_1, d_2, J_2, \ldots, d_\ell, J_\ell)$. Then, the second criterion can be stated as follows:

$$\phi_p = \left[\sum_{i=1}^{\ell} J_i d_i^{-p}\right]^{1/p} \tag{20}$$

where p is a positive integer chosen equal to 15.

Combining Eqs. (17) and (20) into one objective can be an effective way of improving LHD and consequently increases the metamodels performance by minimising the following expression:

$$\Psi = w\rho^2 + (1-w)\phi_p, \tag{21}$$

where w is the weight factor; for simplicity, it is decided to weight the objectives equally.

The problem formulated by Eq. (21) is a typical hard optimisation problem to be solved mostly when the number of factors and sample size increase due to the combinatorial explosion of possible solutions. A modified version of the SA algorithm is used to solve the previous problem due to its global search ability. Compared with the classical SA algorithm, the modification lies in the perturbation operator, where an exchange mechanism is used to make the perturbation from the current LHD. It should be noted that there are many ways to perturbate LHD randomly. In our contribution, we use an exchange procedure to explore the search space which consists in choosing randomly one column in the range [1,ζ] and two elements between [1,n_v] within that column which are exchanged to find a new design. The SA algorithm starts with random LHD and an initial temperature T and generate a sequence of configurations denoted by n_t which represents the number of trials in each temperature level. The iterative procedure can be described as follows: given a random LHD denoted by $\mathcal{D}_i$ with cost function $\Psi(\mathcal{D}_i)$, the next LHD $\mathcal{D}_j$ is generated based on an exchange procedure described previously. If $\big(\Psi(\mathcal{D}_j) - \Psi(\mathcal{D}_i)\big) \leq 0$, the new LHD is accepted, otherwise, in the case when the difference is greater than zero, the new state will be accepted with the probability:

$$\Pr(\cdot) = \exp\left(\frac{\Psi(\mathcal{D}_i) - \Psi(\mathcal{D}_j)}{T}\right) > \xi$$

where ξ is an integer random number generated with uniform distribution in the range [0,1].

This property promotes a better exploration of the search space by accepting the worse LHD with specific probability given above. Then, the temperature is decreased and the new number of steps to be performed of the temperature level is determined and the process is repeated. For updating temperature, the logarithmic update function is adopted. The proposed algorithm can be easily implemented even for large sample size but with significant increase in CPU time and iterations number for convergence. It should be noted that the required number of iterations to achieve better LHD is exponentially dependent on the sample size. For large sample size, it is obvious that the algorithm may become prohibitively expensive in terms of both computational and memory requirements. For this work, the stopping criterion is defined as the maximum number of iterations conducted which is set to 5,000. In the framework of this study, it is found to suffice to guarantee a LHD with improved properties.

In order to demonstrate the effectiveness of the above algorithm, we take a random LHD with two factors and 16 sampled points as an example. The modified version of the SA algorithm described above is implemented through iterative subroutine developed in MATLAB R2008a environment [29]. Subpanels a and b of Fig. 1 display, respectively, the random and the optimal LHD which show significant improvements in terms of both the correlation and the inter-sites distances criterions. Obviously, the exchange mechanism appears very efficient to make an effective search. The improved LHD would be satisfactory for enhancing the metamodels accuracy. This procedure is implemented in the rest of this paper for generating LHDs to construct the required metamodels.

2.4 Test function

To investigate the prediction capability of the RSM and the LSSVR metamodelling techniques, test function from literature [30] has been chosen to compare their performance prediction as their goodness-of-fit in particular when the real function is nonlinear. The following test function is proposed to conduct the comparison analysis:

$$f(\mathbf{x_1}, \mathbf{x_2}) = 2 + \exp\left(\frac{-\mathbf{x_1}^2}{10}\right) + \left(\frac{\mathbf{x_2}}{5}\right)^4 - \mathbf{x_1} \tag{22}$$

where $\mathbf{x_1}$ and $\mathbf{x_2}$ are truncated Gaussian distribution variables.

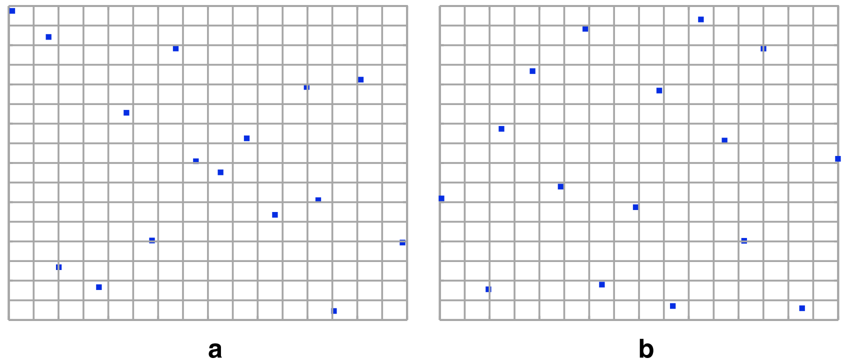

Fig. 1 Comparison between **a** the random LHD ($\phi_p = 0.6424$, $\rho^2 = 0.3767$) and **b** the improved LHD ($\phi_p = 0.2749$, $\rho^2 = 0.0134$)

To evaluate the metamodels performance, three error measures including the root mean square error (RMSE), the maximum absolute error (MAE) and the coefficient of determination R^2 are used for accuracy assessment. The mathematical definition of these criterions is summarised in Table 1. The RMSE quantifies the deviation between the predicted and the real data while the MAE provides a measure of the relative overall fit. Smaller (RMSE, MAE) means that the metamodel output is accurate and exactly matches with the real data. R^2 is a measure of the amount of reduction in the variability of the predicted output. R^2 close to unity indicates that the model can explain well all the variability of the predicted data. In this work, we examined two cases for comparing the RSM and the LSSVR metamodelling techniques: when the sample size used to identify the metamodel is small and large. Optimisation procedure detailed in the previous subsection is applied to obtain the optimal LHD used to construct the metamodels.

Table 1 summarises the error measures values for the different metamodelling techniques. It is obvious that the LSSVR with PL and RBF kernel functions yields accurate results with both small and large sample size. From Table 1, we can see that the LSSVR(PL) provides practically the same performance prediction capability as the LSSVR(RBF). In contrast, the RSM seems not suitable even with large sample size. In addition, we can see that with the RSM, increasing the number of sampled points will not necessarily lead to a more accurate metamodels. In contrast, the LSSVR metamodels become more and more accurate. One may observe that the standard error (RMSE and MAE) goes to zero at the sampled points, indicating that we have practically no uncertainty about the predicted values. The results show as well the superiority of the RBF kernel function compared to the PL one.

In order to compare the goodness-of-fit, we plot in subpanels a and b of Fig. 2 the contour line of the real function and those obtained with the metamodels with both small and large sample size, respectively. We can see that the RS metamodels oversimplify the real function and is unable to better capture the nonlinear behaviour which produce substantial errors in the prediction. In contrast, the LSSVR fits very well the real function even with small sample size.

By extending the use of the generated metamodels in optimisation framework, this may present a serious problem. One may observe that the fitted quadratic surface is unreliable because the surface not sufficiently capture the shape of the real function. Notice that the minimum of the quadratic surface does not even lie close to the function minima. This example shows the drawbacks of the RS metamodel which can fail to provide reliable optimum in optimisation procedure. From literature, several authors have been shown that even with iterative improvements of

Table 1 Performance measures analysis: comparison between the RS and the LSSVR metamodels

Indicator	Equation[a]	Sample size	Metamodelling technique		
			RSM	LSSVR(PL)	LSSVR(RBF)
R^2	$1-\frac{\sum_{i=1}^{n_v}(y_i-\hat{y}_i)^2}{\sum_{i=1}^{n_v}(y_i-\bar{y})^2}$	25	0.9409	0.9997	0.9999
		150	0.8966	0.9999	0.9999
RMSE	$\sqrt{\frac{1}{k}\sum_{i=1}^{n_v}\left(y_i-\hat{y}_i\right)^2}$	25	1.2008	0.0814	8.0285e-004
		150	1.3887	0.0514	0.0369
MAE	$\underset{i=1,\ldots,n_v}{\mathrm{Max}}\left(\lvert y_i-\hat{y}_i\rvert\right)$	25	2.1116	0.1951	0.0022
		150	3.5892	0.1097	0.0783

[a]Where y, $\hat{y}$ and $\bar{y}$ are the real, predicted and mean values, respectively, and n_v is the sample size

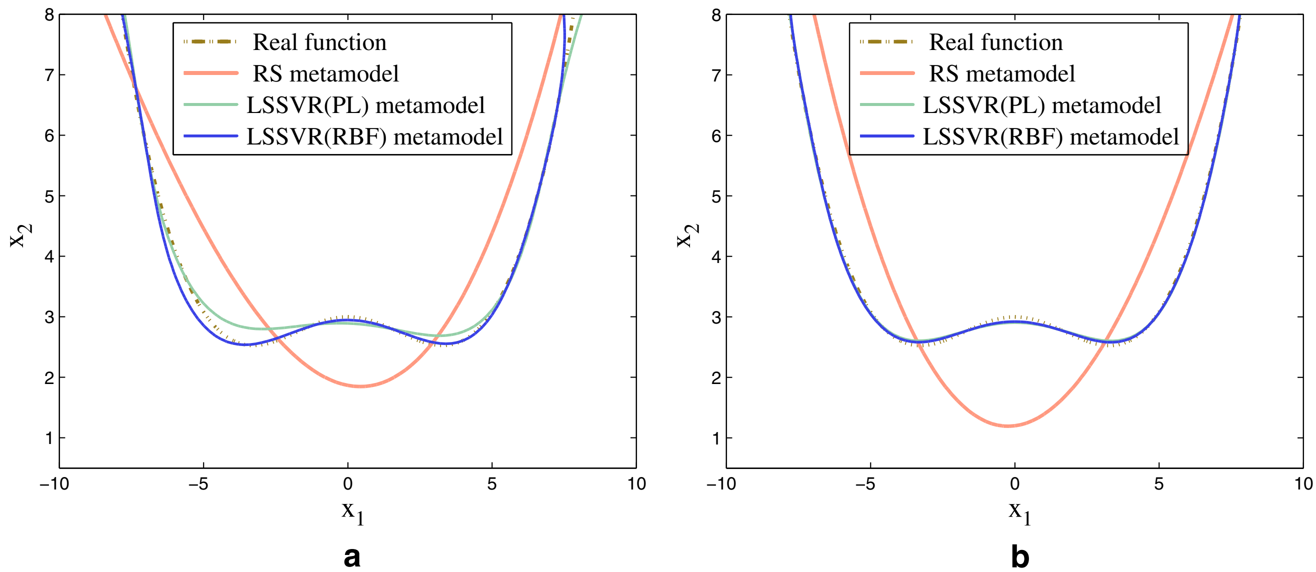

Fig. 2 Comparison between metamodelling techniques with **a** small and **b** large sample size

the quadratic response surface, it is hard to converge "near" to the global optimum.

From comparison study including performance error measures and graphical analysis, the LSSVR with both PL and RBF kernel functions has shown its potential in producing statistically superior results to the RSM as demonstrated through the proposed test function. This comparison is now conducted for practical industrial problem as the THF process before proceeding for optimisation using the generated metamodels. As known, the process involves several sources of nonlinearities originating from material behaviour, geometry and applied loads.

3 Application to the THF process

3.1 Finite element model

Figure 3a shows a half FE model that was defined to simulate the THF process. It is composed of the die that represents the desired part, punches and tube. The FE mesh of the tube is shown in Fig. 3b; due to the symmetric character of the THF process, only a quarter of the model is used which is composed of 1,340 elements. Shell elements with five integration points through the shell section called S4R are employed to mesh the tube. The tools are meshed with four-node, bilinear quadrilateral, rigid elements, called R3D4. To simulate the process, we use the explicit dynamic FE code Abaqus\Explicit [31]. A coulomb friction coefficient of 0.15 is used to simulate the friction behaviour between the contact surfaces of the tube and the die. The parameters of the FE model (mesh, mass scaling and contact algorithm) are selected after several numerical simulations to evaluate their influence on the computational time and to achieve good results. Table 2 summarises the dimensions characteristics of the tube and the die used for FE simulations.

3.2 Material properties

In this study, Swift hardening law given by Eq. (23) is used to characterise the material behaviour:

$$\bar{\sigma} = K(\varepsilon_0 + \bar{\varepsilon})^n, \tag{23}$$

where K is the strength coefficient value, n is the work hardening exponent and ε_0 is the pre-strain. $\bar{\sigma}$ and $\bar{\varepsilon}$ are equivalent plastic stress and equivalent plastic strain, respectively.

In order to analyse accurately the THF process, the free bulge test is adopted to determine the material properties

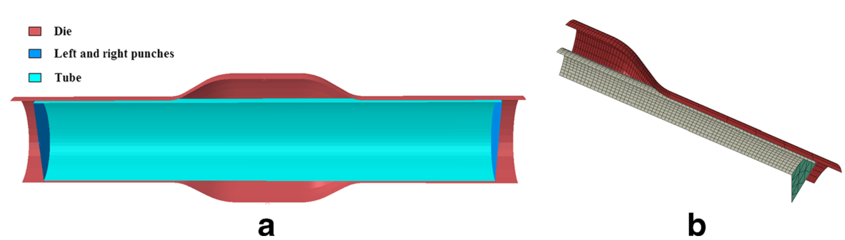

Fig. 3 **a** A half finite element model, **b** mesh used for numerical simulations

Table 2 Tube and die dimensions

Parameters	Designation	Value	Unit
L_0	Tube length	100	mm
D_0	Outside tube diameter	19	mm
t_0	Tube initial thickness	1	mm
r_c	Die corner	8	mm

as the state of stress conditions is similar to the THF process. Table 3 summarises the material properties used for FE simulations [32].

3.3 Selection of the loading path

A careful attention is crucial to select the suitable loading path for the THF process to guarantee a defects-free part. Applied loading path is dependent primarily on the following: the material properties, the shell thickness, the tube diameter as the die shape. The experimental investigations lead to the conclusion that the formability phase can be split into three stages: yielding, expansion and calibration stages. Each stage is characterised by a certain level of internal pressure and axial displacement rate. The initial loading path can be approximated based on the operator experience or by trial-and-error procedure. Koç and Altan [33] proposed to rely three components of pressure based on the knowledge of the material and the geometrical parameters: yield pressure p_y, expansion pressure p_e and calibration pressure p_c. By estimating the previous quantities, one can construct a preliminary loading path that can be used as an initial guess for optimisation procedure. For axial displacement, since the part geometry is simple, it is easy to approximate an initial values. In the present work, the bounds of design variables are adjusted according to the theoretical equations and some FE simulations. The operating ranges for each design variable are summarised in Table 4.

Table 3 Material properties

Properties	Designation	Value	Unit
σ_y	Yield strength	215.18	MPa
ϱ	Material density	7800	kg/m^3
E	Young's modulus	210	GPa
K	Strength coefficient	514.66	MPa
n	Strain hardening exponent	0.362	–
ν	Poisson coefficient	0.3	–
ε_0	Pre-strain	0.0904	–

Table 4 The proposed levels of loading variables

Levels	p_y (MPa)	p_e (MPa)	p_c (MPa)	d_a (mm)
Lower bound	15	25	45	4
Nominal values	20	32.5	52.5	6
Upper bound	25	40	60	8

3.4 Failure modes in the THF process

The possible failure modes in THF process are necking and wrinkling. Wrinkling occurs when we apply an excessive axial displacement combined with low pressure level. Figure 4a shows the tube shape as the most critical regions when the wrinkling phenomenon may initiate. Those regions are identified by maximum values of the plastic strain. One may observe that the wrinkles localised in the form of an outward bulge where very high local strains appeared in these waves. The same phenomenon was observed experimentally in numerous studies [34, 35] as shown in Fig. 4b. As it can be seen, the FE model reproduces accurately all aspects of the wrinkling phenomenon. It should be noted that in practice, the wrinkles are influenced by many factors such as the mechanical properties of the material, the geometry of the die and the frictional conditions. This plastic instability is usually observed during initial and intermediate stages of the THF process. In contrast, failure caused by necking appears when we apply a high level of pressure combined with low axial displacement and is observed at an advanced stage of the process. The FE model shows that the bursting may occur in the middle of the expanded zone as predicted by the numerical simulation based on the fracture index (see Fig. 5a). The FE simulation reveals that the maximum fracture index occurs usually at the element located in the middle of the expanded zone. The bursting location observed experimentally for the same geometry was shown in the literature in several works [36, 37] as shown in Fig. 5b which confirms the numerical prediction. Consequently and in order to avoid occurrence of plastic instabilities, the usual objective is to find a tradeoff between the applied internal pressure and the axial displacement rate.

To control the process, numerous criterions were proposed in the literature to prevent wrinkling and necking plastic instabilities. For wrinkling, criterions based onto geometrical considerations are widely applied due to their simple mathematical formulations. However, those criterions are limited for components with simple geometry. The FLD expressed in terms of limit major and minor in-plane components of true strain is widely used in metal forming processes for both wrinkling and necking failure modes [38, 39]. If critical levels of strain are attained during the forming process, necking or wrinkling of the material occurs. It

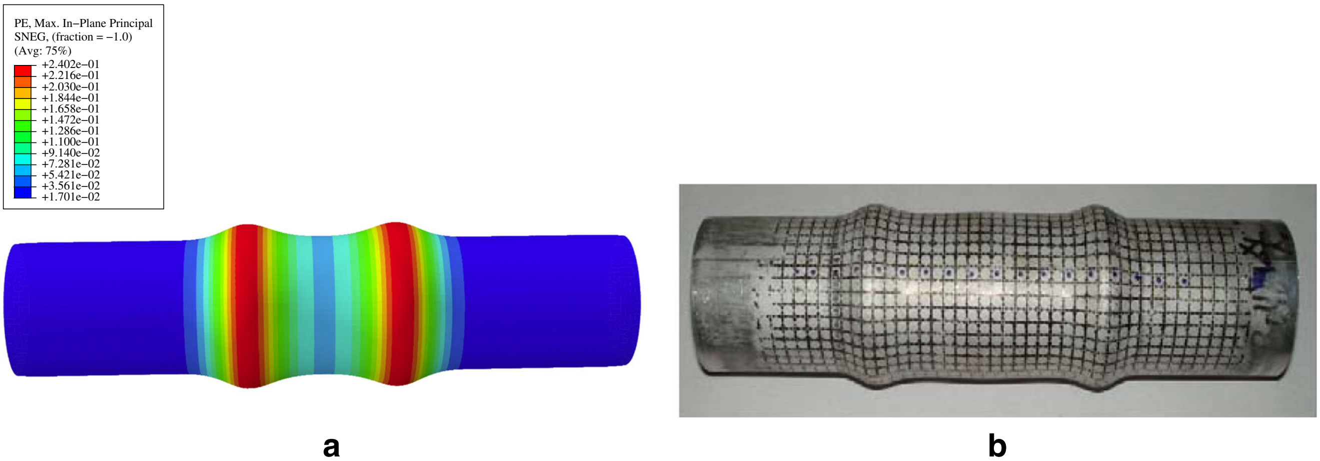

Fig. 4 **a** Plastic strain distribution: wrinkles locations, **b** wrinkles initiation zone observed with experiment [34]

is worth to mention that the FLD is reliable only in processes in which the loading path is linear which is not the case for THF process. In the study of Stoughton [40], it has been shown that the forming limit stress diagram (FLSD) is insensitive by changes to the strain path. This property makes the FLSD an attractive alternative to the FLD for the prediction of necking instability under arbitrary loading (i.e. proportional and non-proportional loads).

3.5 Definition of the objective functions

In metal forming processes, the objective functions can be formulated in a different manner which depend on the required specifications and performances desired by the designer. These objective functions may include uniform thickness distribution, shape conformity or damage distribution among others. Those objectives may be in conflict with each other; for this reason, multi-objective optimisation appears the appropriate formulation to find the tradeoffs between them. In the present work, three objective functions will be defined to control the process. The first one consists in minimising the tube wall thickness variation which is defined as follows:

$$F_{\text{thin}}(\mathbf{x}) = \sqrt{\sum_{i=1}^{n_e} \left(\frac{t_i - t_0}{t_0} \right)^2} \tag{24}$$

where t_0 is the initial thickness, t_i is the thickness of the ith element at the end of the process, n_e is the number of elements and $\mathbf{x} = (p_y, p_e, p_c, d_a)$ is the vector of design variables to be optimised.

To avoid necking occurrence, we define an objective function which take advantage from the FLSD obtained experimentally [32]. As the experimental process involves several sources of uncertainties which may affect the FLSD position, safety margin concept which is frequently used in practice is defined. Based on the FLSD, we distinguish mainly two regions: feasible region below the lower margin curve when THF process can be done in secure conditions and unfeasible one above the upper margin curve when plastic instabilities occur (see Fig. 6). The implementation of the FLSD damage initiation criterion in the FE code requires the specification of the major principal in-plane stress at damage initiation as tabular function of the minor principal in-plane stress. The damage initiation criterion is met when the condition $w_{\text{FLSD}} = 1$ is satisfied, where the variable

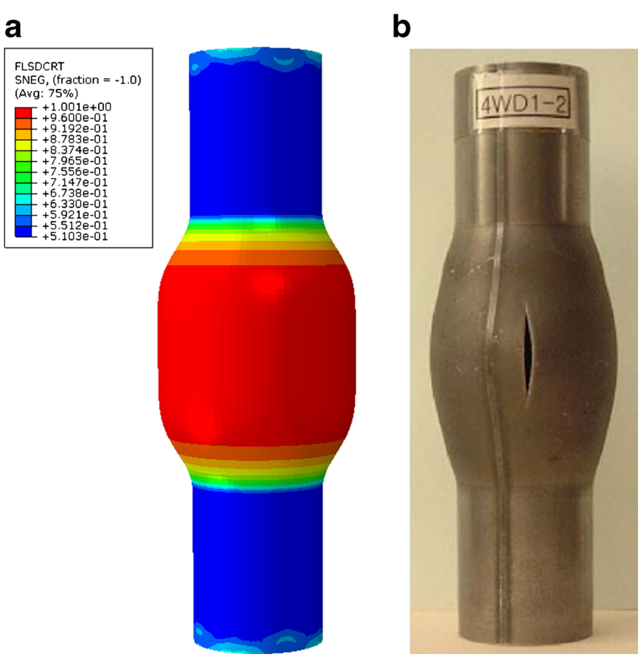

Fig. 5 **a** Fracture index evaluated with the FE model **b** experimental bursting failure [36]

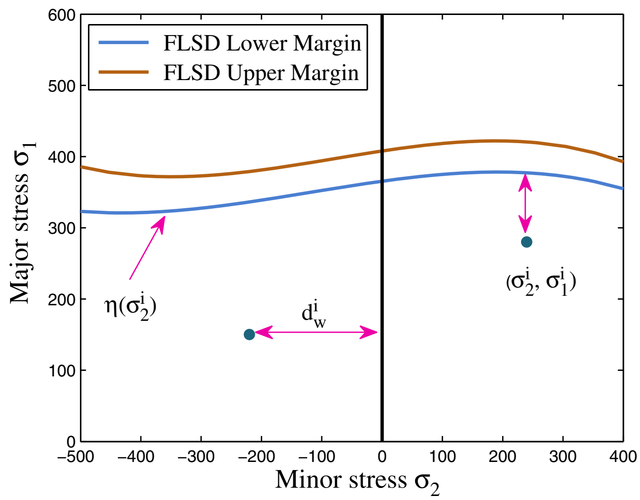

Fig. 6 Definition of the objective function for necking and wrinkling based on the FLSD

w_{FLSD} given by Eq. (25) is a function of the current stress state and is defined as the ratio of the current major principal stress σ_{major} to the major stress on the FLSD $\sigma_{\mathrm{major}}^{\mathrm{FLSD}}$ evaluated at the current values of minor stress, σ_{minor}:

$$w_{\mathrm{FLSD}} = \frac{\sigma_{\mathrm{major}}}{\sigma_{\mathrm{major}}^{\mathrm{FLSD}}} = \frac{\sigma_1}{\eta\left(\sigma_2\right)} \tag{25}$$

where $\eta(\cdot)$ is a polynomial model given the major stress as a function of the minor stress.

It should be noted that Abaqus FE code evaluates the FLSD criterion using the stresses averaged through the thickness of the element. Based on Eq. (25), the second objective function is defined to ensure a uniform stress distribution by minimising the following expression:

$$F_{\mathrm{nec}}(\mathbf{x}) = \sum_{i=1}^{n_e}\left(\frac{\sigma_1^i}{\eta(\sigma_2^i)} - 1\right)^2 \tag{26}$$

In order to minimise the wrinkling tendency, an objective function inspired from the FLSD is defined as well. The risk of wrinkling is higher when the tube is in a state of in-plane compression. Thus, the proposed criterion consists in minimising the distances between the compressive minor stresses from the line where $\sigma_2 = 0$ (see Fig. 6). Mathematically, the proposed objective function can be stated as follows:

$$F_{wr}(\mathbf{x}) = \begin{cases} \frac{1}{20n_e}\sum\limits_{i=1}^{n_e} \mid d_w^i \mid = \frac{1}{20n_e}\sum\limits_{i=1}^{n_e} \mid \sigma_2^i \mid & if \quad \sigma_2^i < 0 \\ 0 & if \quad \sigma_2^i \geq 0 \end{cases} \tag{27}$$

It should be noted that for this criterion evaluation, the objective function values are multiplied by $(1/20n_e)$ in order to make them in the same order of magnitude as the previous ones and to avoid possible problems related to different scales.

From a practical point of view, the above objective functions are frequently considered for optimising various metal forming processes. To construct metamodels for the different objective functions, we use an optimal LHD obtained through the iterative procedure described in Section 2.3 which is composed of 25 sampled points. FE simulations are performed using an Intel(R) Core(TM) 2 Duo CPU with 2.26 GHz processor and 4 GB RAM. Table 5 summarises

Table 5 Performance measures analysis: comparison between the proposed metamodelling techniques

Indicator	Equation[a]	Response	Metamodelling technique RSM	LSSVR(PL)	LSSVR(RBF)
R^2	$1 - \frac{\sum_{i=1}^{n_v}\left(y_i - \hat{y}_i\right)^2}{\sum_{i=1}^{n_v}\left(y_i - \bar{y}\right)^2}$	F_{thin}	0.9855	0.9999	0.9999
		F_{nec}	0.9889	0.9993	0.9999
		F_{wr}	0.7402	0.7683	0.9999
RMSE	$\sqrt{\frac{1}{k}\sum_{i=1}^{n_v}\left(y_i - \hat{y}_i\right)^2}$	F_{thin}	0.1254	3.2255×10^{-5}	0.0091
		F_{nec}	0.1110	0.0278	1.0777×10^{-7}
		F_{wr}	7.5014	6.2483	0.0010
MAE	$\underset{i=1,\ldots,n_v}{\mathrm{Max}}\left(\lvert y_i - \hat{y}_i\rvert\right)$	F_{thin}	0.3029	9.8507×10^{-5}	0.0263
		F_{nec}	0.2927	0.0885	2.7550×10^{-7}
		F_{wr}	22.7558	15.6114	0.0035

[a] Where y_i, $\hat{y}_i$ and $\bar{y}$ are the real, predicted and mean values, respectively, and n_v is the sample size

the error measures used to evaluate the metamodels predictability. We can see that the LSSVR(RBF) metamodels is the most accurate one based on the error measures. Hence, through the rest of this manuscript, the LSSVR(RBF) metamodels will be used for GSA and to make a comparison with the RS metamodels for optimisation. We can see that the RS and the LSSVR(PL) metamodels are unable to better capture the wrinkling phenomenon. Obviously, due to the high nonlinear nature of this plastic instability and the high-order interactions effects.

4 Global sensitivity analysis

In this section, we will introduce the GSA and then discuss the obtained results. First of all, we have to make a distinction between local sensitivity analysis and GSA. Most of the published papers dealing with sensitivity analysis in metal forming processes concern the local sensitivity analysis in which one factor at a time is varied and the others are kept constant at their nominal values. In our contribution, we propose a GSA which evaluates the effect of one parameter while the others are varying as well. This method is more complicated and more demanding in terms of computational effort. In addition, it requires metamodels with high precision to be effective and reliable. Recently, several methods was proposed in the literature to conduct sensitivity analysis in various engineering problems. The most popular are: the sampling-based methods [41], the derivative-based methods [42] and the variance-based method considered in the present work. The GSA helps to identify accurately the most influential parameters involved in the process. Additionally, it provides a better explanation on how perturbation affecting each design variable may impact the variance of the quality functions defined to control the process. For GSA, the LSSVR(RBF) is preferred since it provides metamodels with high quality as shown previously by means of several error measures. The proposed method presents two major advantages: it is based only on model evaluations and easy to implement.

To deal with GSA, we associate some scatter to the defined design variables. This is more realistic since in manufacturing processes, such variables are defined with a certain degree of accuracy. Let assume that the design variables are defined with truncated Gaussian distribution where the lower and the upper bounds are defined previously in Table 4. Table 6 summarises the statistical characteristics of the random variables considered in the present study: it should be noted that the coefficient of variation (COV) might be the same for all variables and it also might be different for every variable, depending on the designer knowledge. In the following, the former case is considered.

Table 6 Statistical properties of random design variables

Variable	Mean value	COV(%)	Distribution type
p_y	20	10	Gaussian
p_e	32.5	10	Gaussian
p_c	40	10	Gaussian
d_a	6	10	Gaussian

4.1 Variance-based method

The variance-based GSA can quantify the first-order and total effect on the variance of model output. Let us consider a model $Y = f(\boldsymbol{\theta})$, where Y is the model output, $\boldsymbol{\theta} = (\theta_1, \theta_2, \ldots, \theta_s)$ is the input parameters vector. A variance decomposition of f suggested by Sobol' [43] is given as follows:

$$V(Y) = \sum_{i=1}^{s} V_i + \sum_{i=1}^{s} \sum_{j=i+1}^{s} V_{ij} + \ldots + V_{1,\ldots,s} \tag{28}$$

$V(Y)$ is the total unconditional variance, V_i is the partial variance or main effect of θ_i on Y and given by $V_i = V[E(Y|\theta_i)]$ (where $E(Y|\theta_i)$ denotes the expectation of Y on θ_i), V_{ij} is the joint impact of θ_i and θ_j on the total variance minus their first-order effects.

Saltelli et al. [44] introduced the first-order sensitivity index S_i and total effect sensitivity index S_i^{TOT} given by Eqs. (29) and (30), respectively:

$$S_i = \frac{V_i}{V(Y)} = \frac{V[E(Y|\theta_i)]}{V(Y)} \tag{29}$$

$$S_i^{\mathrm{TOT}} = S_i + \sum_{j \neq i} S_{ij} + \ldots = \frac{E[V(Y|\theta_{\sim i})]}{V(Y)} \tag{30}$$

where $\theta_{\sim i}$ denotes variation on all input parameters except θ_i, and S_{ij} is the contribution to the total variance by the interactions between parameters.

In order to compute S_i and S_i^{TOT}, an efficient method proposed by Saltelli et al. [45] is used. It consists in creating two independent input parameters sampling matrices $\mathcal{A}$ and $\mathcal{B}$ with dimensions (N, s), where N is the sample size and s is the number of input parameters. Each row in matrix $\mathcal{A}$ and $\mathcal{B}$ represents a possible value of θ. The Monte Carlo approximations for $V(Y)$, S_i and S_i^{TOT} are defined as follows:

$$\hat{f}_0 = \frac{1}{N} \sum_{j=1}^{N} f(\mathcal{A})_j \tag{31}$$

$$\hat{V}(Y) = \frac{1}{N} \sum_{j=1}^{N} (f(\mathcal{A})_j)^2 - \hat{f}_0^2 \tag{32}$$

Table 7 First- and high-order sensitivity indices

Variable	F_{thin}		F_{nec}		F_{wr}	
	$\hat{S}_i$	$\hat{S}_i^{TOT}$	$\hat{S}_i$	$\hat{S}_i^{TOT}$	$\hat{S}_i$	$\hat{S}_i^{TOT}$
p_y	0.0579	0.0684	0.9007	0.9492	0.0116	0.2747
p_e	0.0054	0.0125	0.0063	0.0427	0.1199	0.3337
p_c	0.0081	0.0354	0.0042	0.0241	0.0182	0.1163
d_a	0.8877	0.9245	0.0125	0.1428	0.5326	0.6248
$\sum_i \hat{S}_i \Big/ \sum_i \hat{S}_i^{TOT}$	0.9591	1.0408	0.9237	1.1588	0.6823	1.3495

$$\hat{S}_i = \frac{1}{N} \sum_{j=1}^{N} \frac{f(\mathcal{B})_j \left(f\left(\mathcal{A}_{\mathcal{B}}^{(i)}\right)_j - f(\mathcal{A})_j \right)}{\hat{V}(Y)} \tag{33}$$

$$\hat{S}_i^{TOT} = \frac{1}{2N} \sum_{j=1}^{N} \frac{\left(f(\mathcal{A})_j - f\left(\mathcal{A}_{\mathcal{B}}^{(i)}\right)_j \right)^2}{\hat{V}(Y)} \tag{34}$$

where $\hat{\ldots}$ denotes the estimate, $\hat{f}_0$ is the estimated value of the model output, $\mathcal{A}_{\mathcal{B}}^{(i)}$ represents all columns from $\mathcal{A}$ except the ith column which is from $\mathcal{B}$.

We generated a quasi random sequence matrix of size $(N, 2s)$, where $\mathcal{A}$ and $\mathcal{B}$ are the left and right half of this matrix, respectively.

4.2 Discussion

Table 7 summarises the first- and high-order sensitivity indices which shows how variation in design variables may affect the variance of the objective functions defined to control the THF process. By analysing the sensitivity indices obtained for the first objective function, one may observe that the variation of the axial displacement affects considerably the thickness distribution variance. The first-order index for d_a, $\hat{S}_{d_a} = 0.8877$ represents the fractional contribution of d_a (i.e. its main effect) to the thickness distribution variability. In contrast, variation affecting yielding, expansion and calibration pressures affects slightly the thickness distribution, their contribution is less than 8 %. Thickness

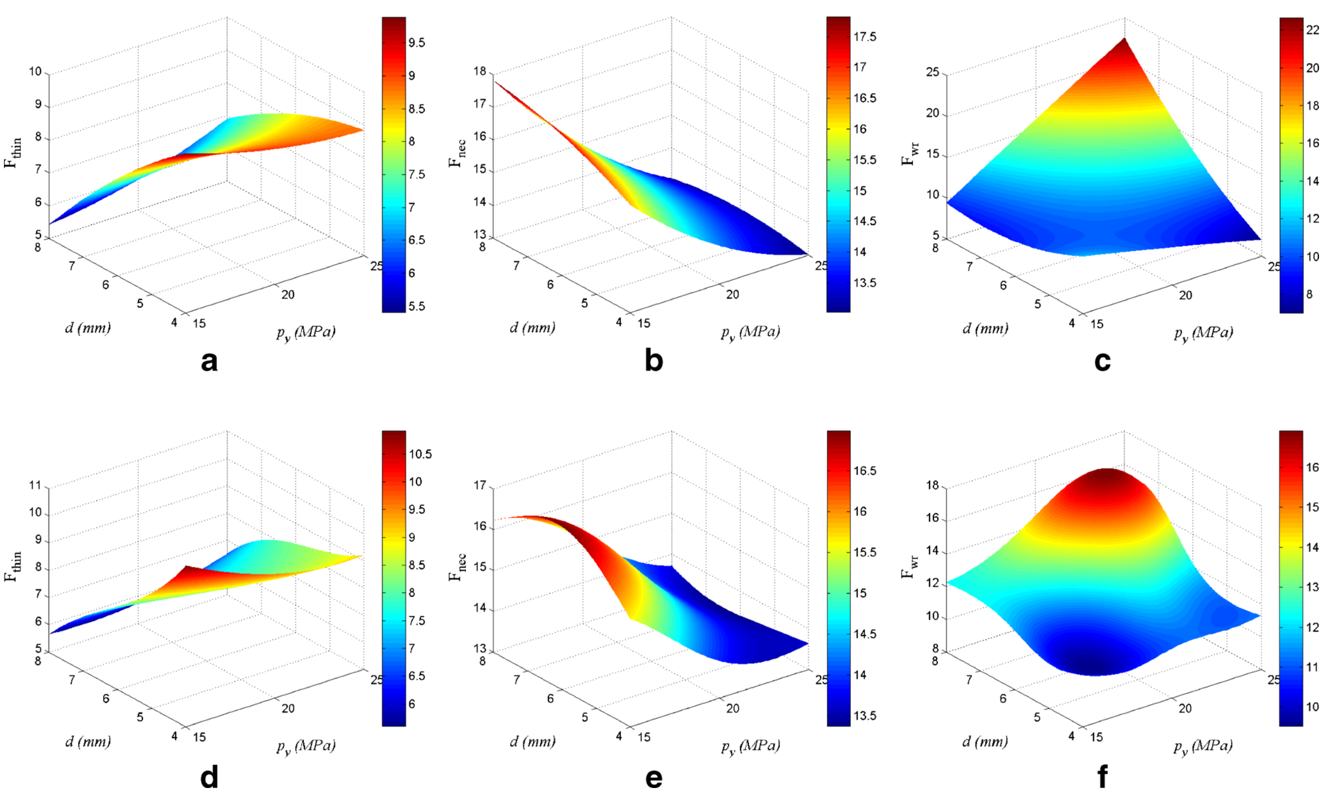

Fig. 7 Comparison between objective functions obtained with **a**–**c** the RS and **d**–**f** the LSSVR(RBF) metamodels

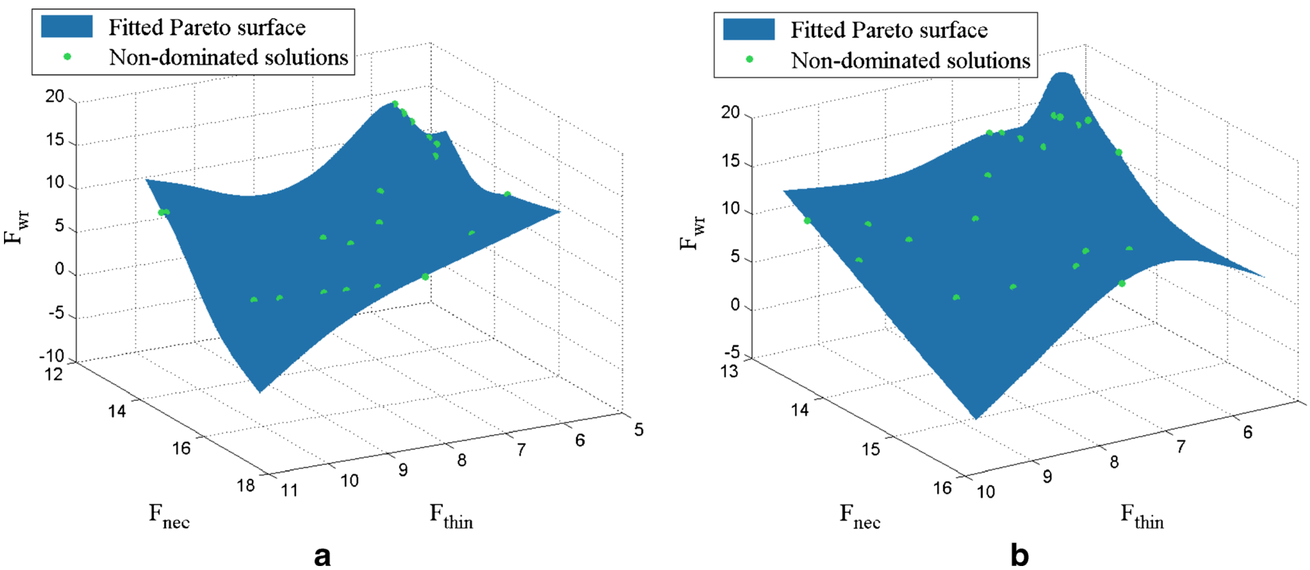

Fig. 8 Pareto optimal solutions and fitted Pareto surface obtained with **a** the RS and **b** the LSSVR(RBF) metamodels

distribution seems to behave almost additively as the sum of all the $\hat{S}_i$'s is very close to 1 (0.9591).

Now let us analyse the sensitivity of necking objective function. We can see that for the first-order sensitivity indices, yielding pressure is the most influential variable, 90.07 % of the necking objective variance is explained by single contribution of the previous variable. For high-order sensitivity, we can see that 14.28 % of the variance is explained by the contribution of the axial displacement. Variation which may affect expansion and calibration pressures seems to affect slightly the necking response. One may observe that 92.37 % of the necking output variance is explained by single contribution of the loading path design variables. For necking, axial displacement d_{a} is found important only for its high-order interactions $\left(\hat{S}_{d_{\mathrm{a}}}^{\mathrm{TOT}} - \hat{S}_{d_{\mathrm{a}}} = 0.1303\right)$.

For wrinkling objective function, one may observe from Table 7 that expansion pressure and axial displacement are the dominant variables which may affect the wrinkling variance. Expansion as calibration pressures impact the wrinkling response by approximately the same proportion. We can see that the difference between the total effect and the first-order index of p_y, $\hat{S}_{p_y}^{\mathrm{TOT}} - \hat{S}_{p_y} = 0.2631$, indicates that 26.31 % of the output variance is accounted for by interactions in which p_y is involved. This means that p_y interacts with other input parameters but it does indicate with which parameters these interactions occur. It should be noted that wrinkling is influenced by some high-order interactions, as seen by the sum of $\hat{S}_i^{\mathrm{TOT}}$, which is greater than 1 ($\hat{S}_i^{\mathrm{TOT}} = 1.3495$). This result confirms the non-suitability of the RS as the LSSVR(PL) metamodels to better capture the wrinkling phenomenon due to the higher order effects.

GSA reveals that variation which may affect the loading path variables have significant effect on the variance of the defined objective functions and consequently on the quality of the hydroformed part. One may conclude that variation in axial displacement affects considerably the thickness distribution and wrinkling objective functions. In contrast, necking objective function appears very sensitive to the yielding pressure. Additionally, we can see that wrinkling phenomenon is impacted by some high-order interactions. The above results show that all the design variables should be controlled during the manufacturing process due to the interaction effects to avoid potential failure occurrence and to guarantee hydroformed parts with high mechanical properties.

5 Multi-objective optimisation of the THF process

5.1 Optimisation problem formulation

Before dealing with optimisation, let us compare the general shape of the objective functions provided by the different metamodelling techniques. Subpanels a–c and d–f of Fig. 7 show in three-dimensional space the objective functions obtained with the RS and the LSSVR(RBF) metamodels, respectively. By comparing the same objective function

Table 8 Performance measures metrics for the optimal Pareto fronts

Metric	SP	$\mathcal{G}(\mathcal{P}_r, \mathcal{P}_l)$	$\mathcal{G}(\mathcal{P}_l, \mathcal{P}_r)$
Pareto front (RSM)	0.9350	0	0.8811
Pareto front (LSSVR(RBF))	0.5612		

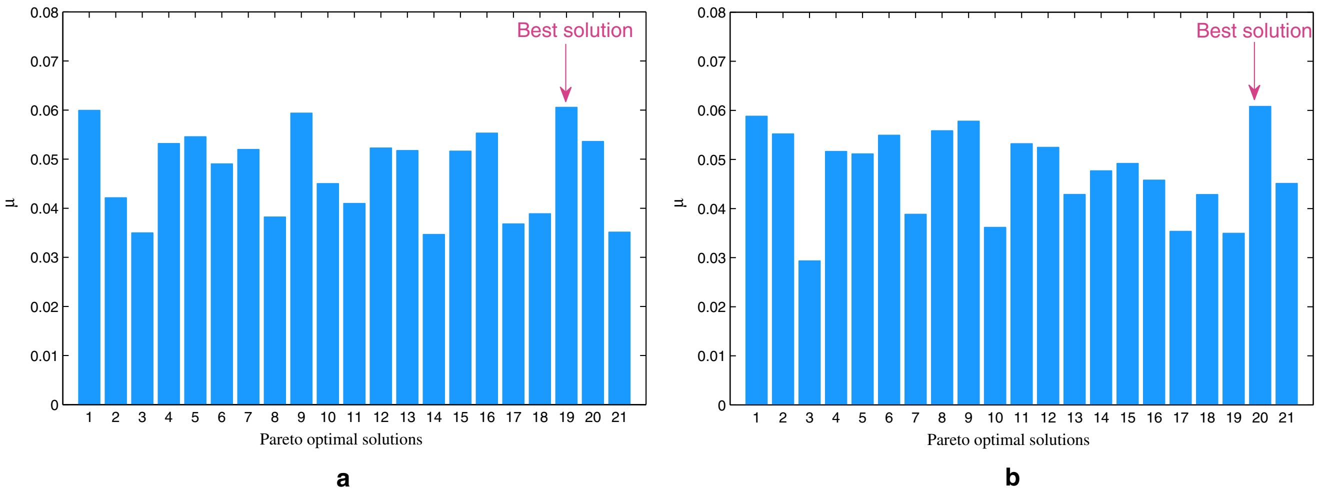

Fig. 9 Fuzzy classification of the Pareto optimal solutions **a** RSM **b** LSSVR(RBF)

obtained with RS and LSSVR(RBF) metamodels, one may observe that the general shape is different. In addition, we can see the differences in the objective functions ranges in the color map where the lowest values are dark blue and the highest values are dark red. For wrinkling, one may observe that the RS metamodel predicts the objective function values with a relatively larger error, consequently the algorithm may fail to converge near to the "true" Pareto front and may affect considerably the quality of the obtained solutions.

Now let us formulate the multi-objective optimisation problem which can be stated as follows:

$$\begin{aligned} &\underset{\mathbf{x}}{\text{Minimise}} \quad F = [F_{\text{thin}}(\mathbf{x}), F_{\text{nec}}(\mathbf{x}), F_{wr}(\mathbf{x})] \\ &\text{subject to}: \ \mathbf{x}^l \leq \mathbf{x} \leq \mathbf{x}^u \end{aligned} \tag{35}$$

where F is the vector of the objective functions and $\mathbf{x}^l$, $\mathbf{x}^u$ are the lower and upper bounds, respectively, imposed on the design variables.

To solve the problem formulated by Eq. (35), various algorithms are proposed in the literature. In this work, the Non-dominated Sorting Genetic Algorithm (NSGA-II) [46] which has successfully solved various complicated real-world problems is used. Metamodels generated by the RSM and the LSSVR(RBF) are used to solve the problem in order to analyse the robustness of each optimal Pareto front by comparing several performance metrics detailed in the next subsection. Subpanels a and b of Fig. 8 show the Pareto optimal solutions as the fitted Pareto surface in the objective space obtained with the RS and the LSSVR(RBF) metamodels, respectively.

5.2 Performance measures metrics of the Pareto fronts

Let us compare the Pareto fronts obtained based on the RS and the LSSVR(RBF) metamodels using two different performance metrics to judge about the robustness of each one. It should be noted that the proposed performance metrics was basically used in the literature to compare the performance of the Pareto fronts issued from different multi-objective algorithms. Some of these metrics require the knowledge of the "true" Pareto front; in our selection, we limited ourselves on those which are independent on the "true" Pareto front. The performance metrics used in this paper are described as follows:

- The first metric proposed by Schott [47] consists in measuring the spread of the non-dominated solutions throughout the Pareto front. Let us denote by q the number of solutions in the non-dominated Pareto set and n_f is the number of objective functions. The first metric is expressed as follows:

$$SP = \sqrt{\frac{1}{q-1}\sum_{i=1}^{q}\left(1-\frac{d_i}{\bar{d}}\right)^2} \tag{36}$$

Table 9 Comparison between the FE and the predicted values computed by the RS and the LSSVR(RBF) metamodels

	RS			LSSVR(RBF)		
	F_{thin}	F_{nec}	F_{wr}	F_{thin}	F_{nec}	F_{wr}
FE model	5.9118	13.9667	11.9147	5.8822	13.3863	11.6031
Predicted values	5.4876	13.0383	9.6264	5.8507	13.2087	11.5168
Relative error (%)	7.1800	6.6500	19.2100	0.5400	1.3300	0.7400

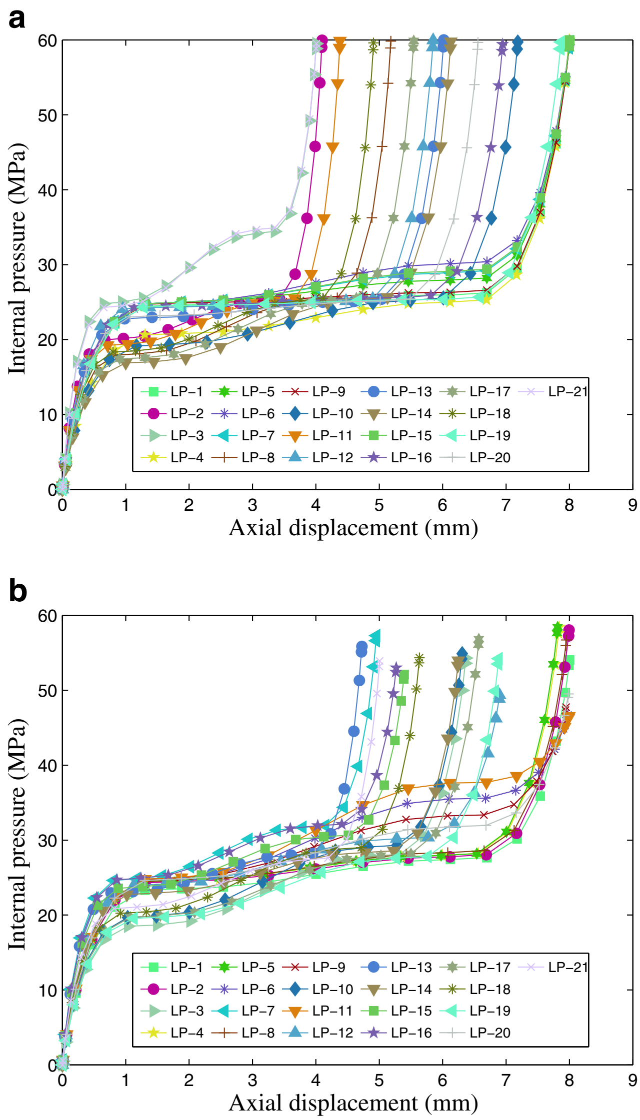

Fig. 10 Optimal loading paths obtained with **a** RS and **b** LSSVR(RBF) metamodels

where $d_i = \min_v \sum_{m=1}^{n_f} \mid F_m^i - F_m^v \mid$, $v = 1, \ldots, q$ and $i \neq v$, $\bar{d}$ is the mean of all d_i.

A value of zero for this metric indicates the ideal diversity that all member of the Pareto front are equidistantly and uniformly spaced. A smaller value of SP is preferable.

- The second metric is the generalizational distance [48, 49] in which the distance between a dominated solution and its corresponding nearest solution has been considered in the objective function space. It measures how far a solution is relative to another one. Let us denote by $\mathcal{P}_r$ and $\mathcal{P}_l$ two Pareto sets, obtained by using the RS and the LSSVR(RBF) metamodels, respectively and ℓ the number of dominated solutions from a Pareto set $\mathcal{P}_l$

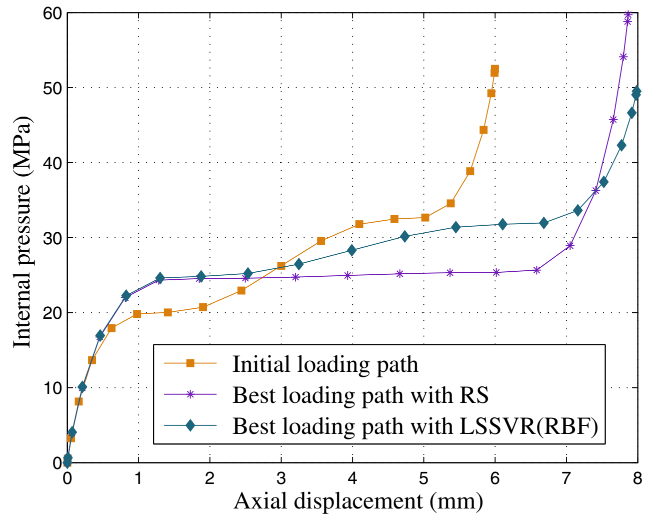

Fig. 11 Comparison between optimal loading paths

by at least one solution from a Pareto set $\mathcal{P}_r$. Each dominated solution in $\mathcal{P}_l$ searches its nearest solution in the objective function space in $\mathcal{P}_r$. The difference in each objective function of a solution vector is raised to power γ and summed up. The obtained values for each dominated solution are raised to power $(1/\gamma)$ and then they are summed up to obtain the generalizational distance, $\mathcal{G}$. Mathematically, $\mathcal{G}$ is defined as:

$$\mathcal{G}(\mathcal{P}_r, \mathcal{P}_l) = \frac{\left(\sum_{j=1}^{\ell}\left(\sum_{i=1}^{n_f}\Delta d_{ij}^2\right)^{\gamma/2}\right)^{1/\gamma}}{\ell} \quad (37)$$

$\Delta d_{ij} = (F_i(\mathcal{P}_r) - F_i(\mathcal{P}_l))$ of the jth dominated solution of the Pareto set $\mathcal{P}_l$. $F_i(\mathcal{P}_l)$ implies the ith objective function value in the Pareto set $\mathcal{P}_l$ and $F_i(\mathcal{P}_r)$ is the corresponding objective function from the nearest solution in Pareto set $\mathcal{P}_r$. γ is an index with integer value.

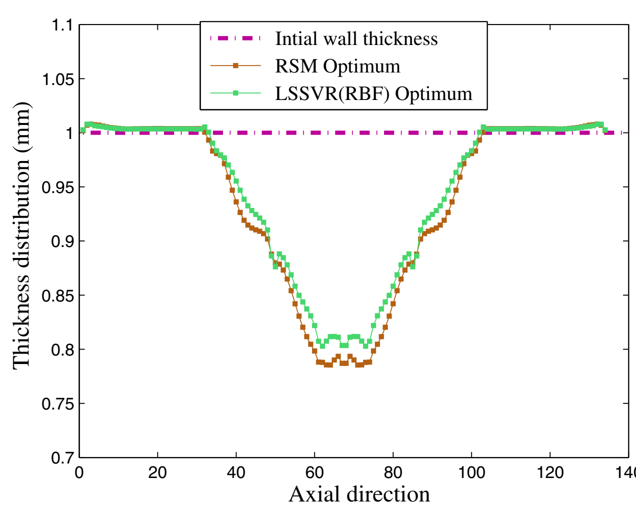

Fig. 12 Comparison between the tube wall thickness distribution

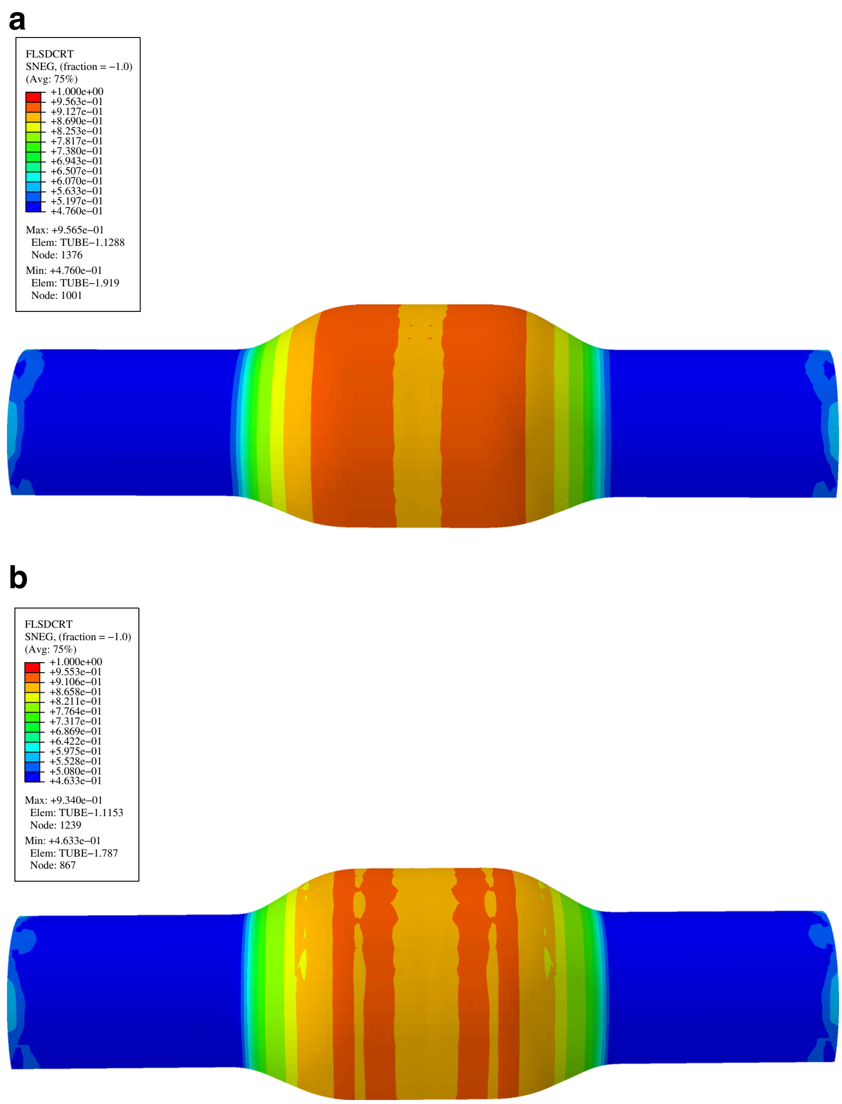

Fig. 13 FLSD criterion values at the end of the process **a** RSM **b** LSSVR(RBF)

If the value of $\mathcal{G}(\mathcal{P}_r, \mathcal{P}_l)$ is more than $\mathcal{G}(\mathcal{P}_l, \mathcal{P}_r)$, then it can be said that the Pareto set $\mathcal{P}_r$ is a better approximation of the true Pareto set than the Pareto set $\mathcal{P}_l$. The difference in $\mathcal{G}(\mathcal{P}_r, \mathcal{P}_l)$ and $\mathcal{G}(\mathcal{P}_l, \mathcal{P}_r)$ values gives a quantitative measurement.

To provide a quantitative measure that describe the quality of the Pareto fronts obtained with both RS and LSSVR(RBF) metamodels, the previous metrics are evaluated. Table 8 summarises the values of the different metrics obtained for each Pareto front. It should be noted that the following metrics are evaluated only for the final non-dominated solutions and not for all generations during optimisation iterative process. It is revealed that the Pareto front provided by the LSSVR(RBF) metamodels is completely superior to the one obtained based on the RS metamodels considering the different metrics. It appears that the multi-objective optimisation based on the LSSVR(RBF) metamodels find good solutions and a good spread of solutions across the front. Consequently, we can admit that the Pareto front obtained by the LSSVR(RBF) is more close to the "true" Pareto front.

5.3 Results and analyses

5.3.1 Fuzzy classification of the Pareto set solutions

A question that is often raised in practice is whether to select the best solution from the non-dominated ones for real manufacturing process. To answer to this question, we use the fuzzy classification of the Pareto set solutions which allows quick ranking of solutions without additional simulations. This technique can be very useful and very helpful for designers and decision makers, but such choice is not necessarily the best alternative, the designer has to try several techniques to decide on the best one for the problem under

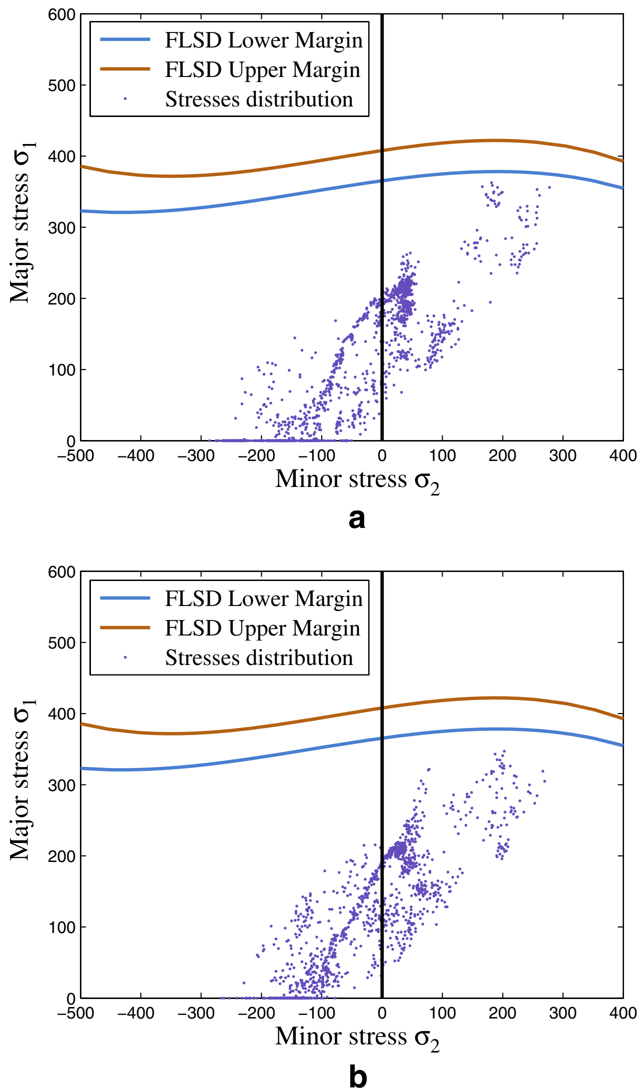

Fig. 14 Stress distribution obtained with **a** RS and **b** LSSVR(RBF) best loading path

consideration. In order to guide the designer selection, it is assumed that there is fuzziness in the goal of each objective. In the present work, we use fuzzy decision making proposed by Panigrahia et al. [50] to classify the Pareto optimal solutions and to find the best compromise solution. This fuzziness is defined by membership function which represent the degree of fuzziness in some fuzzy sets using values in the range of [0,1]. The proposed membership function is defined as follows:

$$\mu_i^j = \begin{cases} 1 & if \quad F_i \le F_i^{\min} \\ \frac{F_i^{\max} - F_i}{F_i^{\max} - F_i^{\min}} & if \quad F_i^{\min} < F_i \le F_i^{\max} \\ 0 & if \quad F_i > F_i^{\max} \end{cases} \tag{38}$$

where μ_i^j indicates how well the jth non-dominated solution is able to satisfy the ith objective. The sum of membership values for all objectives of the jth non-dominated solutions suggests how well it satisfies all the objectives. The achievement of each non-dominated solution can be with respect to all the q non-dominated solutions and can be obtained as follows:

$$\mu^j = \frac{\sum_{i=1}^{n_f} \mu_i^j}{\sum_{j=1}^{q} \sum_{i=1}^{n_f} \mu_i^j} \tag{39}$$

The solution with maximum value of μ^j is the compromised solution that can be accepted by the decision maker. Subpanels a and b of Fig. 9 show the solutions which constitute the front Pareto with their respective μ^j values for both RSM and LSSVR(RBF), respectively. It can be seen that for the RSM, the 19th solution is the best one with high value of μ^j while for LSSVR(RBF), the 20th one is the best. It means that those solutions provide the best trade-off between the defined objective functions. After ranking the solutions issued from the proposed metamodelling techniques, let us make a deep comparison between the best ones which provide the ideal compromise and their effect on the hydroformability of the tube based on the desired specifications.

5.3.2 Comparison between the best RS and the LSSVR(RBF) optimums

To verify the accuracy of the metamodels at the selected optimum solutions. FE simulations with those optimal loading paths are carried out to make a comparison with the predicted values. Table 9 summarises the obtained values as the relative errors obtained for each metamodel. One may observe that the predicted values based on the LSSVR(RBF) metamodels are in good agreement with that from the FE simulations. In contrast, significant relative errors is observed with the RS metamodels mostly for the wrinkling response. This may induce a substantial errors for metamodels predictions and consequently affect the solutions robustness.

Subpanels a and b of Fig. 10 show, respectively, the optimal loading paths (LPs) obtained for the non-dominated solutions obtained by RS and LSSVR(RBF) metamodels as discretised by the FE code. For numerical simulations, the loading path is divided into 20 equal increments and the loading rate is uniform for both axial displacement and internal pressure. Figure 11 shows the initial loading path and the best ones obtained by the fuzzy classification method for each metamodelling technique. One may

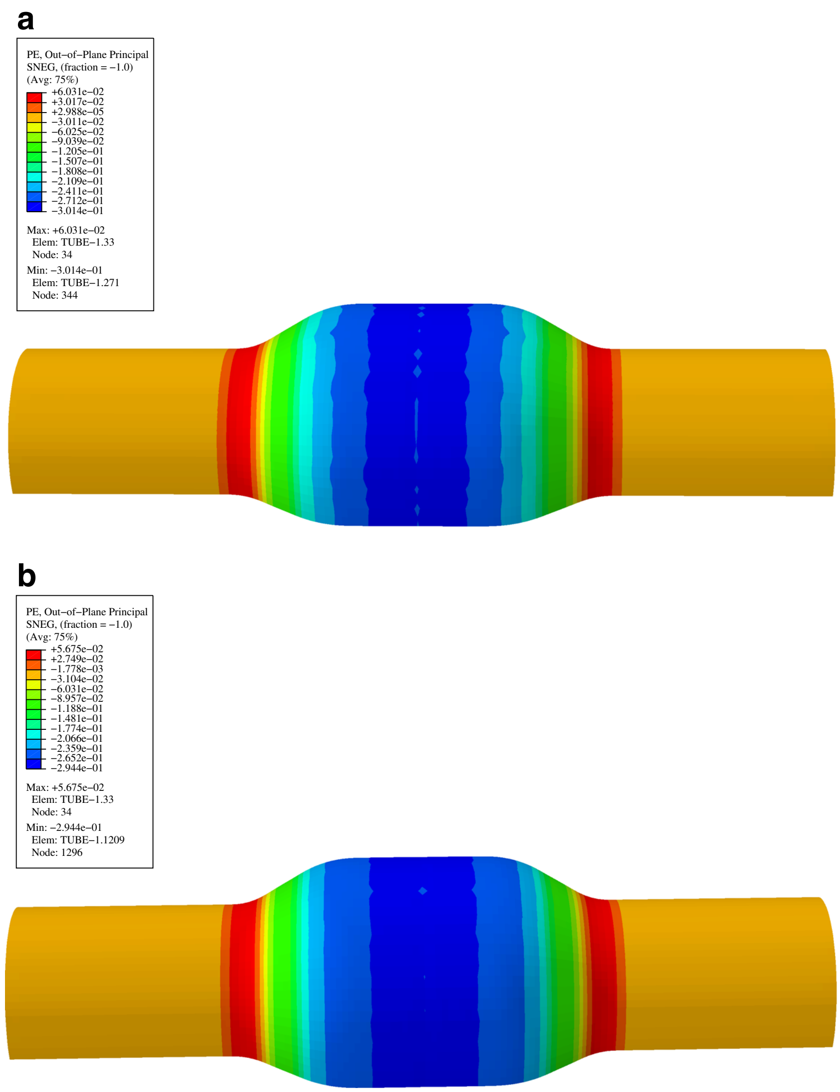

Fig. 15 Out-of-plane plastic strain contour obtained with **a** RS and **b** LSSVR(RBF) best loading path

observe that the loading paths are quite similar at the beginning of the process. However, for the LSSVR(RBF), optimal loading path an increase in the expansion pressure is observed while a relatively small increase is shown for the RSM optimal loading path. In contrast, at the final stage, the calibration pressure is decreased for the LSSVR(RBF) optimal loading path. Compared with the initial loading path, we can see that more axial displacement rate is required for both optimums to push material into the die cavity to guarantee the degree of conformity and to improve the thickness distribution.

Let us compare the tube wall thickness distribution obtained with each optimal loading path selected previously. Based on Fig. 12, one may observe that with the LSSVR(RBF) loading path, a uniform thickness distribution is guaranteed mainly at the expanded region when the probability of necking occurrence is higher. The gain in reduction rate in wall thickness distribution is significant compared with the RSM. Percentage in thinning ratio drops down to 19.71 % with the optimal loading path obtained based on the LSSVR(RBF) metamodels while it is equal to 21.45 % with the one obtained using the RS metamodels.

Subpanels a and b of Fig. 13 show the resulting FLSD criterion values at the end of the THF process obtained with the best solutions based on the RS and LSSVR(RBF) metamodels, respectively. It should be noted that the onset of instability is reached when the FLSD criterion is equal to 1. The corresponding maximum FLSD criterion values are 0.9565 and 0.9340 based on RS and LSSVR(RBF) metamodels, respectively.

Comparing the stress distribution in the minor–major space (based on Fig. 14a,b), we can see that for both RSM and LSSVR(RBF), major and minor stress distribution are below the lower safety margin. However, one may observe that the lowest stress range is obtained with the optimum provided by the LSSVR(RBF) metamodels. The

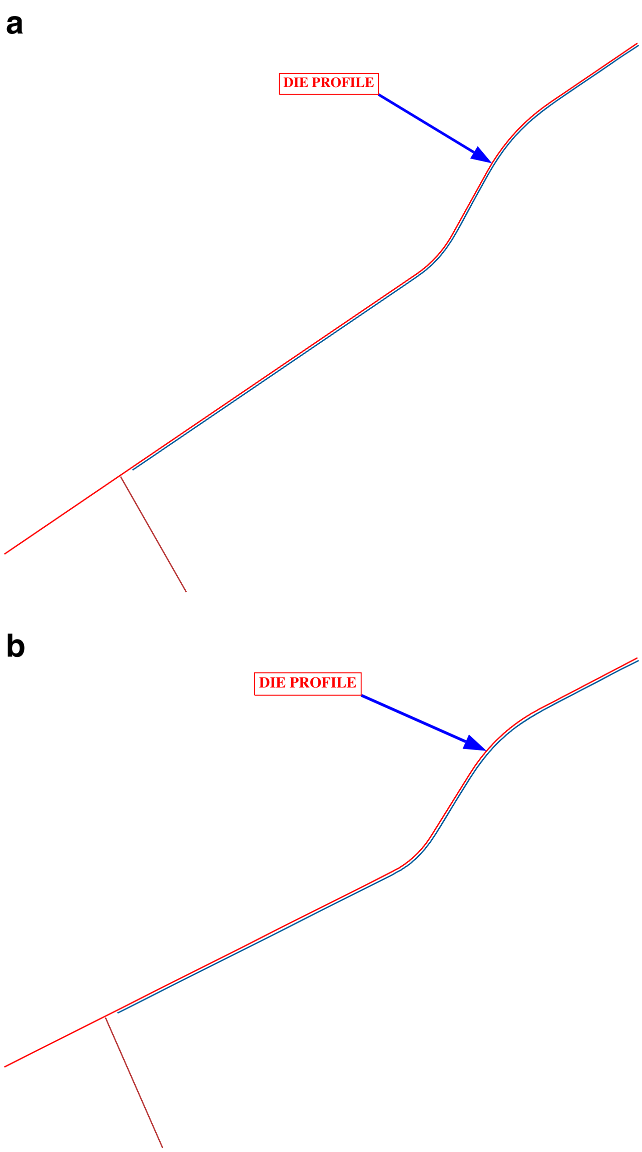

Fig. 16 Degree of shape conformity obtained with **a** RS and **b** LSSVR(RBF) best loading path

LSSVR(RBF) optimal loading path leads to a smaller major stress at the critical element. For the RS loading path, the maximum major stress reaches 363 MPa while it is equal to 347 MPa with the LSSVR(RBF) optimum. For the minor stress, the absolute maximum stress is decreased by 16 MPa with the LSSVR(RBF) optimum. This indicates that the LSSVR(RBF) optimum leads to a significant improvement in the THF process deformation mechanics.

In order to compare the wrinkling tendency for both optimums, Fig. 15a,b show the out-of-plane plastic strain contour and deformed tube. One may observe that loading path obtained by using the LSSVR(RBF) metamodels provides less out-of-plane plastic strain which better for wrinkling prevention.

By verifying the degree of shape conformity, one may observe (see Fig. 16a,b) that for both optimums, the tubes fill perfectly the die shape; however, better thickness distribution and less deformation severity are achieved with the optimal loading path obtained using the LSSVR(RBF) metamodels.

Based on the obtained results, one may conclude that the high performance of the metamodels is reflected in the quality of the solutions achieved. Optimisation of the THF process based on the RSM suffers from the inaccuracies of metamodels due to the approximation errors associated with metamodels. It seems that the high nonlinear nature of the THF process requires metamodels with high performances to better optimise the process. The degree of accuracy achieved by the RS metamodels seems insufficient to provide a good approximation of the true Pareto front; in contrast, the LSSVR(RBF) metamodels provide better Pareto front as was shown based on the performance metrics. For this reason, it is advisable to use more sophisticated metamodelling techniques for better capturing the nonlinear phenomenons involved in the THF process. Moreover, the presence of nonlinearities in the objective functions give raise to non-convexity issues which represent the limitations of the RSM. Due to the high precision of describing the involved phenomenons in THF process, multi-objective optimisation coupled with the LSSVR(RBF) shows its ability of searching high quality solutions.

6 Concluding remarks

This research provides a deep comparison between the RSM and the LSSVR as metamodelling techniques to construct metamodels for global sensitivity analysis and multi-objective optimisation of the THF process. The LSSVR shows its superiority over the RSM to deal with nonlinearities proved through analytical test function and practical industry problem as THF process. The main advantages of the LSSVR technique lies in its ability to conduct optimisation strategy and global sensitivity analysis with high accuracy. In contrast, the RSM shows several limitations due to the errors of approximation associated to the metamodels. On the other side, the GSA reveals that thickness distribution and wrinkling are highly sensitive to the axial displacement while necking appears very sensitive to the yielding pressure. This can provide guidance for designer to better control the process in order to guarantee hydroformed components with high mechanical properties and minimise the rejection rate in a mass production environment. In addition, optimisation of the THF process based on the LSSVR(RBF) metamodels yields to significant improvements in thickness as stress distribution; moreover, the wrinkling tendency is as well minimised. With the help of some performance metrics, it has been found that the quality of a Pareto set of solutions obtained based on the LSSVR(RBF) metamodels is better than the ones using RS metamodels. One may conclude that the LSSVR(RBF) based on improved LHD can be an effective alternative to determine optimal loading path for the THF process than the RSM which was widely used in metal forming processes as already mentioned. The RSM presents several limitations and the LSSVR seems the best alternative to deal with GSA and optimisation in hydroforming processes when various sources of nonlinearities exist.

Our future research consists in extending the use of the LSSVR in multi-objective optimisation with uncertainty consideration applied for the THF process. This will be done in order to investigate how uncertainties may affect the location as the shape of the Pareto front since imprecise knowledge of process parameters including material properties, geometric characteristics and loads are often encountered in a mass production environment.

References

1. Oh SI, Jeon BH, Kim HY, Yang JB (2006) Applications of hydroforming processes to automobile parts. J Mater Proc Technol 174:42–55
2. Dohmann F, Hartl Ch (2004) Hydroforming-applications of coherent FE-simulations to the development of products and processes. J Mater Proc Technol 150:18–24
3. Palumbo G (2013) Hydroforming a small scale aluminum automotive component using a layered die. Mater Des 44:365–373
4. Ray P, Mac Donald BJ (2004) Determination of the optimal load path for tube hydroforming processes using a fuzzy load control algorithm and finite element analysis. Finite Elem Anal Des 41:173–192
5. An H, Green DE, Johrendt J (2010) Multi-objective optimization and sensitivity analysis of tube hydroforming. Int J Adv Manuf Technol 50:67–84
6. Ingarao G, Di Lorenzo R, Micari F (2009) Internal pressure counter punch action design in Y-shaped tube hydroforming processes: a multi-objective optimisation approach. Comput Struct 87:591–602
7. Lin FC, Kwan CT (2004) Application of abductive network and FEM to predict an acceptable product on T-shape tube hydroforming process. Comput Struct 82:1189–1200
8. Mirzaalia M, Liaghata GH, Moslemi Naeinia H, Seyedkashia SMH, Shojaeeb K (2011) Optimization of tube hydroforming process using simulated annealing algorithm. Procedia Eng 10:3012–3019
9. Xu X, Zhang W, Li S, Lin Z (2009) Study of tube hydroforming in a trapezoid-sectional die. Thin-Walled Struct 47:1397–1403
10. Zadeh HK, Mashhadi MM (2006) Finite element simulation and experiment in tube hydroforming of unequal T shapes. J Mater Proc Technol 177:684–687
11. Alaswad A, Benyounis KY, Olabi AG (2011) Employment of finite element analysis and response surface methodology to investigate the geometrical factors in T-type bi-layered tube hydroforming. Adv Eng Softw 42:917–926
12. Abedrabbo N, Worswicka M, Mayerb R, Van Riemsdijkc I (2009) Optimization methods for the tube hydroforming process applied to advanced high-strength steels with experimental verification. J Mater Proc Technol 209:110–123
13. Di Lorenzo R, Ingarao G, Chinesta F (2009) A gradient-based decomposition approach to optimize pressure path and counter punch action in Y-shaped tube hydroforming operations. Int J Adv Manuf Technol 44:49–60
14. Wei D, Cui Z, Chen J (2008) Optimization and tolerance prediction of sheet metal forming process using response surface model. Comput Mater Sci 42:228–233
15. Bahloul R, Ben-Elechi S, Potiron A (2006) Optimisation of springback predicted by experimental and numerical approach by using response surface methodology. J Mater Proc Technol 173:101–110
16. Hu W, Yao LG, Zhi-Hua Z (2008) Optimization of sheet metal forming processes by adaptive response surface based on intelligent sampling method. J Mater Proc Technol 197:77–88
17. Azaouzi M, Lebaal N (2012) Tool path optimization for single point incremental sheet forming using response surface method. Simul Model Pract Theory 24:49–58
18. Tang B, Sun J, Zhao Z, Chen J, Ruan X (2006) Optimization of drawbead design in sheet forming using one step finite element method coupled with response surface methodology. Int J Adv Manuf Technol 31:225–234
19. Naceur H, Ben-Elechi S, Batoz JL, Knopf-Lenoir C (2008) Response surface methodology for the rapid design of aluminum sheet metal forming parameters. Mater Des 29:781–790
20. Ingarao G, Di Lorenzo R, Micari F (2009) Analysis of stamping performances of dual phase steels: a multi-objective approach to reduce springback and thinning failure. Mater Des 30:4421–4433
21. Alaswad A, Benyounis KY, Olabi AG (2011) Employment of finite element analysis and response surface methodology to investigate the geometrical factors in T-type bi-layered tube hydroforming. Adv Eng Softw 42:917–926
22. Di Lorenzo R, Ingarao G, Chinesta F (2010) Integration of gradient based and response surface methods to develop a cascade optimisation strategy for Y-shaped tube hydroforming process design. Adv Eng Softw 41:336–348
23. Alaswad A, Olabi AG, Benyounis KY (2011) Integration of finite element analysis and design of experiments to analyse the geometrical factors in bi-layered tube hydroforming. Mater Des 32:838–850
24. Hasanpour F, Ensafi AA, Khayamian T (2010) Simultaneous chemiluminescence determination of amoxicillin and clavulanic acid using least squares support vector regression. Anal Chim Acta 670:44–50
25. Hea K, Laib KK, Yenc J (2012) A hybrid slantlet denoising least squares support vector regression model for exchange rate prediction. Procedia Comput Sci 1:2397–2405
26. Lin KP, Pai PF, Lu YM, Chang PT (2013) Revenue forecasting using a least-squares support vector regression model in a fuzzy environment. Inf Sci 220:196–209
27. Farquad MAH, Ravi V, Bapi Raju S (2010) Support vector regression based hybrid rule extraction methods for forecasting. Expert Syst Appl 37:5577–5589
28. Morris MD, Mitchell TJ (1995) Exploratory designs for computational experiments. J Stat Plan Infer 43:381–402
29. MATLAB R (2008) The MathWorks Inc., Natick
30. Zhiwei G, Guangchen B (2008) Application of least squares support vector machine for regression to reliability analysis. Chin J Aeronaut 22:160–166
31. Abaqus Manual (2010) Version 6.10. Dassault systèmes. http://www.simulia.com
32. Song WJ, Heo SC, Ku TW, Jeong K, Kang BS (2010) Evaluation of effect of flow stress characteristics of tubular material on forming limit in tube hydroforming process. Int J Mach Tool Manuf 50:753–764

33. Koç M, Altan T (2002) Prediction of forming limits and parameters in the tube hydroforming process. Int J Mach Tool Manuf 42:123–138
34. Yuan S, Yuan W, Wang X (2006) Effect of wrinkling behavior on formability and thickness distribution in tube hydroforming. J Mater Proc Technol 177:668–671
35. Ze-jun T, Gang L, Zhu-bin H, Shi-jian Y (2010) Wrinkling behavior of magnesium alloy tube in warm hydroforming. Trans Nonferrous Metals Soc China 20:1288–1293
36. Kim J, Kim SW, Song WJ, Kang BS (2004) Analytical approach to bursting in tube hydroforming using diffuse plastic instability. Int J Mech Sci 46:1535–1547
37. Kim J, Kang SJ, Kang BS (2003) A prediction of bursting failure in tube hydroforming processes based on ductile fracture criterion. Int J Adv Manuf Technol 22:357–362
38. Wei L, Yuying Y (2008) Multi-objective optimization of sheet metal forming process using Pareto-based genetic algorithm. J Mater Proc Technol 208:499–506
39. Sun G, Li G, Gong Z, Cui X, Yang X, Li Q (2010) Multiobjective robust optimization method for drawbead design in sheet metal forming. Mater Des 31:1917–1929
40. Stoughton TB (2000) A general forming limit criterion for sheet metal forming. Int J Mech Sci 42:1–27
41. Helton JC, Davis FJ (2000) Mathematical and statistical methods for sensitivity analysis of model output. Wiley, New York
42. Sobol' IM (2001) Global sensitivity indices for nonlinear mathematical models and their Monte Carlo estimates. Math Comput Simul 55:271–280
43. Sobol' IM (1990) On sensitivity estimation for nonlinear mathematical models. Matem Mod 2(1):112–118
44. Saltelli A, Ratto M, Andres T, Campolongo F, Cariboni J, Gatelli D, Saisana M, Tarantola S (2008) Global sensitivity analysis: the primer. Wiley Ltd, New York
45. Saltelli A, Annoni P, Azzini I, Campolongo F, Ratto M, Tarantola S (2010) Variance based sensitivity analysis of model output. Design and estimator for the total sensitivity index. Comput Phys Commun 181:259–270
46. Deb K, Pratap A, Agarwal S, Meyarivan T (2002) A fast and elitist multiobjective genetic algorithm: NSGA–II. IEEE Trans Evol Comput 6:182–197
47. Schott JR (1995) Fault tolerant design using single and multicriteria genetic algorithms. Master's thesis
48. Pulido GT, Coello Coello CA (2004) The micro genetic algorithm 2: towards online adaptation in evolutionary multiobjective optimisation. Col. San Pedro Zacatenco, Mexico: CINVESTAV-IPN, Evolutionary Computing Group, Department of Electrical Engineering, Section of Computation
49. Van Veldhuizen DA (1999) Multiobjective evolutionary algorithms: classifications, analyses and new innovations. PhD Thesis, Department of Electrical and Computer Engineering, Graduate School of Engineering, Air Force Institute of Technology, Wright-Ptterson, AFB, Ohio
50. Panigrahia BK, Pandia VR, Sharmab R, Dasc S, Dasd S (2011) Multiobjective bacteria foraging algorithm for electrical load dispatch problem. Energy Convers Manage 52:1334–1342